arXiv:1508.00006v2 [physics.flu-dyn] 30 Nov 2015

The stability of a rising droplet: an inertialess non-modal growth mechanism

Giacomo Gallino, Lailai Zhu and François Gallaire[1]†

[1]Laboratory of Fluid Mechanics and Instabilities, École Polytechnique Fédérale de Lausanne, Lausanne, CH-1015, Switzerland

Prior modal stability analysis (Kojima *et al.* 1984) predicted that a rising or sedimenting droplet in a viscous fluid is stable in the presence of surface tension no matter how small, in contrast to experimental and numerical results. By performing a non-modal stability analysis, we demonstrate the potential for transient growth of the interfacial energy of a rising droplet in the limit of inertialess Stokes equations. The predicted critical capillary numbers for transient growth agree well with those for unstable shape evolution of droplets found in the direct numerical simulations of Koh & Leal (1989). Boundary integral simulations are used to delineate the critical amplitude of the most destabilizing perturbations. The critical amplitude is negatively correlated with the linear optimal energy growth, implying that the transient growth is responsible for reducing the necessary perturbation amplitude required to escape the basin of attraction of the spherical solution.

1. Introduction

The instability of capillary interfaces has long been an intriguing topic in fluid mechanics. Perhaps one of the earliest investigated interfacial instability phenomena is the Rayleigh-Taylor instability, where a denser fluid located above a lighter one protrudes into the latter due to any arbitrary small perturbation of the initially flat interface. However, this protrusion is not always observed when a droplet rises or sediments into another density-contrasted fluid. According to Hadamard (1911) and Rybzynski (1911), a spherical translating droplet is a solution of this problem in the Stokes regime, regardless of the presence or magnitude of the surface tension. What remains unknown, however, is the existence of other equilibrium shapes of the droplet and the influence of surface tension on the stability of the spherical solution.

Experiments were conducted by Kojima *et al.* (1984) to examine this issue. Two patterns of shape instability were observed: depending on the viscosity ratio λ, a protrusion or an indentation at the rear of droplet was seen to grow with time. Kojima *et al.* (1984) also performed a linear stability analysis assuming that the droplet underwent small deformations. A linear operator depending on the viscosity ratio λ and capillary number Ca (inversely scaling with the surface tension) was derived which governs the linearised droplet shape evolution. It was found that, irrespective of the value of Ca, i.e. even for arbitrary small surface tension, the eigenvalues of the operator had negative real part, pointing to a linearly stable shape. The authors recognized that this linear stability study contradicted their experiments showing instabilities with finite surface tension; Direct numerical simulations (DNS) (Koh & Leal 1989) also reported the unstable shape evolution of slightly disturbed droplets in the presence of sufficient surface tension (Ca < 10). Re-

† Email address for correspondence: francois.gallaire@epfl.ch

cent numerical work has examined the effect of surfactants (Johnson & Borhan 2000) and viscoelasticity (Wu *et al.* 2012) on this scenario.

The contradiction between the theory and experiments/DNS is somewhat reminiscent of the case of the fingering instability of a film flowing down an inclined plane: the experimentally-measured (Huppert 1982; de Bruyn 1992) critical inclination angle triggering instability was found to be well below that obtained from the linear theory. Bertozzi & Brenner (1997) discovered that the traditional spectrum analysis failed to capture the short-time but significant energy amplification of the perturbations near the contact line. They pinpointed the missing mechanism by performing a so-called non-modal analysis, borrowed from the transient growth theory founded and developed in the early 1990s for hydrodynamic stability analysis (Trefethen *et al.* 1993; Reddy & Henningson 1993; Baggett *et al.* 1995), to identify and interpret the short-time energy amplification.

The non-modal tools of stability theory have been used to explain the discrepancies between the theoretically computed critical Reynolds number and the experimentally-observed counterpart in a variety of wall-bounded shear flows (Schmid 2007). The traditional eigenvalue analysis as also used in Kojima *et al.* (1984), i.e. the so-called modal approach, can sometimes fail to interpret real flow dynamics as the spectrum of the linear operator only dictates the asymptotic fate of the perturbations *without* considering their *short-term* dynamics (Schmid & Henningson 2001). The non-modal analysis, in contrast, is able to capture the short-time perturbation characteristics and determine the most dangerous initial conditions leading to the optimal energy growth. In addition to its great success in the traditional hydrodynamic stability analysis, it has been also used to elucidate complex flow instability problems including capillary interfaces (Davis & Troian 2003), thermal-acoustic interactions (Balasubramanian & Sujith 2008; Juniper 2011) and viscoelasticity (Jovanović & Kumar 2010).

In this paper, we perform a non-modal analysis to investigate the shape instability of a rising droplet in an ambient fluid, neglecting inertial effects. After introducing the linearised equations and operator in Sec. 2 and the non-modal approaches in Sec. 3, we demonstrate the existence of transient growth and predict the critical capillary numbers required for instability to become possible in Sec. 4. In Sec. 5, we conduct in-house DNS to compute the nonlinear shape evolutions of the droplets initiated with the linear optimal perturbations and identify the minimal amplitudes leading eventually to instability. We further analyse the relationship between the optimal growth and the critical amplitude of perturbation. We finally examine how the instability pattern is related to the viscosity ratio and propose a phenomenological explanation in Sec. 6.

2. Governing equations and linearisation

We study the dynamics of a buoyant droplet rising in an ambient fluid in the Stokes regime. The droplet is assumed to be axisymmetric and the axis is along the z direction with gravity $\mathbf{g} = -g\mathbf{e}_z$. The two Newtonian immiscible fluids, one carrying the droplet (fluid 2), and the other constituting the droplet (fluid 1) are characterized by different densities $\rho_2 > \rho_1$, inducing (without loss of generality) an upward migration of the droplet. Likewise, their viscosities are μ_2 and μ_1 respectively, with a ratio $\lambda = \mu_1/\mu_2$. The interface between the two fluids has a uniform and constant surface tension coefficient γ. The undeformed state of the droplet is a sphere of radius a and terminal velocity $U_{\text{ter}} = \frac{a^2 g(\rho_2-\rho_1)}{\mu_2}\frac{1+\lambda}{3(1+3\lambda/2)}$ (Leal 2007). We use a and U_{ter} as the reference length and velocity scales, and $\mu_2 U_{\text{ter}}/a$ as the reference scale for p and $\boldsymbol{\sigma}$, the modified pressure (removing

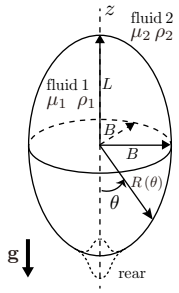

Figure 1: An axisymmetric droplet rising in the quiescent fluid, along the axial (z) direction. The fluid inside and outside is labelled as fluid 1 and fluid 2 respectively, so as their dynamic viscosities (μ_1, μ_2) and densities (ρ_1, ρ_2). The polar coordinates $R(\theta)$ are used to represent its shape, where θ is measured from its rear stagnation point. L and B is the axis length along the revolution axis and orthogonal directions.

the hydrostatic part) and the corresponding stress tensor respectively (Batchelor 2000). Hence, the governing equations for the non-dimensional velocity and pressure field inside the droplet ($\mathbf{u}_1, p_1$) and that outside the droplet ($\mathbf{u}_2, p_2$) are written as

$$\begin{aligned} \nabla \cdot \mathbf{u}_1 = 0, -\nabla p_1 + \lambda \nabla^2 \mathbf{u}_1 = 0, \\ \nabla \cdot \mathbf{u}_2 = 0, -\nabla p_2 + \nabla^2 \mathbf{u}_2 = 0, \end{aligned} \tag{2.1}$$

where the velocity is zero at infinity and the boundary conditions on the interface are

$$\begin{aligned} \mathbf{u}_1 = \mathbf{u}_2, \\ \boldsymbol{\sigma}_2 \cdot \mathbf{n} - \boldsymbol{\sigma}_1 \cdot \mathbf{n} = \left[\nabla \cdot \mathbf{n}/\mathrm{Ca} + 3z\left(1 + 3\lambda/2\right)/\left(1 + \lambda\right)\right]\mathbf{n}. \end{aligned} \tag{2.2}$$

Here, $\mathbf{n}$ is the unit normal vector pointing from the interface towards the carrier fluid and $\mathrm{Ca} = \mu_2 U_{\mathrm{ter}}/\gamma$ is the capillary number indicating the ratio of the viscous effect with respect to the surface tension effect.

Following Kojima *et al.* (1984), the interface of an axisymmetric droplet undergoing small deformation can be expressed in polar coordinates as

$$R(\theta) = 1 + \delta \sum\nolimits_{n=2}^{\infty} (2n+1) f_n P_n(\cos\theta), \tag{2.3}$$

where θ is the polar angle measured from the rear of droplet, $R(\theta)$ is the polar distance (see figure 1), δ indicates the amplitude of the deformation, the P_n are the nth-order Legendre polynomials and the f_n are the corresponding coefficients. The first two terms P_0 and P_1 are removed such that the volume of the droplet is conserved and its centroid stays at the origin (Kojima *et al.* 1984). To advance the interface, the kinematic condition $\partial R(\theta, t)/\partial t = \mathbf{u}(\theta, t) \cdot \mathbf{n}$ is applied.

Following Kojima *et al.* (1984) and linearising the governing equations and truncating the series expansion, the evolution of the droplet can be obtained by solving a system of ordinary differential equations,

$$\mathrm{d}\mathbf{f}/\mathrm{d}t = \mathbf{A}\mathbf{f}, \tag{2.4}$$

where the shape coefficient $\mathbf{f} = (f_2, f_3, ..., f_{m+1})^{\mathrm{T}}$ is a truncated vector and $\mathbf{A}$ is an $m \times m$ matrix depending on λ and Ca. It should be noted that the shape of the droplet can be expressed by a unique series of coefficients $\mathbf{f}\delta$ and vice versa; for a certain $\mathbf{f}$, the effective shape varies significantly with the amplitude and sign of δ. For the truncation

of $\mathbf{f}$ we use $m = 1000$ throughout our study: extensive tests using larger values of m confirm that our results are independent of this truncation level.

3. Non-modal analysis: Theory

As shown by the modal analysis of Kojima *et al.* (1984), the operator $\mathbf{A}$ has a stable spectrum with all of its eigenvalues having negative real parts, irrespective of the magnitude of the surface tension, as long as the capillary number is finite. This model analysis predicts the long-term behaviour of the disturbance but in the short-term limit it is only valid if the linear operator $\mathbf{A}$ is normal, i.e. its eigenvectors are orthogonal. In the case of a non-normal operator, even though the amplitudes of all eigenmodes decay exponentially, their nonorthogonality can lead to a transient energy growth over a short time. We indeed found that $\mathbf{A}$ was non-normal. The optimal growth $G^{\max}$ of the initial energy (L_2 norm) over a chosen time interval $[0, T]$ (Schmid 2007) is

$$G^{\max}(T) = \max_{\mathbf{f}(0)} \left[G(T) = \frac{||\mathbf{f}(T)||_2}{||\mathbf{f}(0)||_2} \right] = ||\exp(T\mathbf{A})||_2, \tag{3.1}$$

where $\mathbf{f}(0)$ denotes the initial perturbation. $G^{\max}(T)$ represents the maximum amplification of the initial energy at a target time (the so-called horizon) T where the optimization has been performed over all possible perturbations $\mathbf{f}(0)$. The optimal initial perturbation for horizon T will be denoted $\mathbf{f}^{\text{opt}}_{[T]}(0)$. The quantity $G^{\max}$ is the envelope of all individual gain profiles, indicating the presence of transient growth when $G^{\max}(T) > 1$ for some T.

Compared with the L_2 norm in equ. 3.1, it is natural to introduce a physically-driven form of energy, designed for the physical problem at hand. In the present study, the variation of surface area of the droplet ΔS is chosen as the target energy, since $\gamma \Delta S$ indicates the interfacial energy throughout the evolution: ΔS is zero only for a spherical droplet and is positive otherwise. The surface area is $S = 2\pi \int_0^\pi R^2 \sin\theta \sqrt{1 + [(1/R)(\partial R/\partial\theta)]^2}\,\mathrm{d}\theta$. Assuming small deformation and thus $\frac{1}{R}\frac{\partial R}{\partial \theta} \ll 1$, a Taylor expansion yields

$$S = 2\pi \int_0^\pi R^2 \sin\theta \left(1 + \frac{1}{2R^2} \left(\frac{\partial R}{\partial \theta} \right)^2 \right) \mathrm{d}\theta. \tag{3.2}$$

Plugging 2.3 into 3.2, the area variation $\Delta S = S - 4\pi$ is found to be

$$\Delta S / \left(2\pi\delta^2\right) = \mathbf{f}^{\mathrm{T}} \mathbf{M}_{\Delta S} \mathbf{f} + o\left(\delta^2\right), \tag{3.3}$$

where $\mathbf{M}_{\Delta S}$ is the so-called weight matrix (Schmid 2001) of size $m \times m$, with entries

$$\mathbf{M}_{\Delta S}(i,j) = 2\delta^{\mathrm{K}}_{ij}(2i+1) + \frac{1}{2}(2i+1)(2j+1) \int_0^\pi P_i'(\cos\theta) P_j'(\cos\theta) \sin^3\theta \mathrm{d}\theta. \tag{3.4}$$

The optimal growth of ΔS can now be defined as

$$G^{\max}_{\Delta S}(T) = \max_{\mathbf{f}(0)} \left[G_{\Delta S}(T) = \frac{\sqrt{\Delta S(T)}}{\sqrt{\Delta S(0)}} \right] = \max_{\mathbf{f}(0)} \left[G_{\Delta S}(T) = \frac{\sqrt{\mathbf{f}^{\mathrm{T}} \mathbf{M}_{\Delta S} \mathbf{f}}}{\sqrt{\mathbf{f}^{\mathrm{T}}(0) \mathbf{M}_{\Delta S} \mathbf{f}(0)}} \right]. \tag{3.5}$$

By Cholesky decomposition $\mathbf{M}_{\Delta S} = \mathbf{F}^{\mathrm{T}}\mathbf{F}$, the above equation is formulated as

$$G^{\max}_{\Delta S}(T) = \max_{\mathbf{f}(0)} \left[G_{\Delta S}(T) = \frac{||\mathbf{F}\mathbf{f}(T)||_2}{||\mathbf{F}\mathbf{f}(0)||_2} \right]. \tag{3.6}$$

In a similar way to how the asymptotic stability ($t \to \infty$) is determined by the eigenvalues of the evolution operator $\mathbf{A}$, the maximum instantaneous growth rate of the perturbation energy at $t = 0^+$ can be determined algebraically, expanding the matrix exponential $\exp(t\mathbf{A}) \approx I + t\mathbf{A}$ at $t = 0^+$. The growth rate of the excess area ΔS is then

$$\frac{1}{\Delta S}\frac{d\Delta S}{dt}\bigg|_{t=0^+} = \frac{\mathbf{f^T}(0)\left[\mathbf{A^T F^T F} + \mathbf{F^T F A}\right]\mathbf{f}(0)}{\mathbf{f^T}(0)\mathbf{F^T F f}(0)}. \tag{3.7}$$

By introducing $\mathbf{h} = \mathbf{F}\mathbf{f}(0)$, the maximum growth rate of ΔS is formulated as

$$\max \frac{1}{\Delta S}\frac{d\Delta S}{dt}\bigg|_{t=0^+} = \max_{\mathbf{h}} \frac{\mathbf{h^T}\left[\mathbf{FAF}^{-1} + \left(\mathbf{FAF}^{-1}\right)^{\mathrm{T}}\right]\mathbf{h}}{\mathbf{h^T h}}, \tag{3.8}$$

which becomes the optimization of a Rayleigh quotient with respect to $\mathbf{h}$. Because $\mathbf{FAF}^{-1} + \left(\mathbf{FAF}^{-1}\right)^{\mathrm{T}}$ is a symmetric operator, the maximum is given by its largest eigenvalue,

$$\max \frac{1}{\sqrt{\Delta S}}\frac{d\sqrt{\Delta S}}{dt}\bigg|_{t=0^+} = s_{\max}\left[\frac{1}{2}\left(\mathbf{FAF}^{-1} + \left(\mathbf{FAF}^{-1}\right)^{\mathrm{T}}\right)\right], \tag{3.9}$$

where $s_{\max}[\cdot]$ denotes the largest eigenvalue. This maximum instantaneous growth rate is commonly called the numerical abscissa (Trefethen & Embree 2005), which is closely linked to the numerical range $W_{\Delta S}(\mathbf{A}, \mathbf{F})$ defined as the set of all Rayleigh quotients,

$$W_{\Delta S}(\mathbf{A}, \mathbf{F}) \equiv \{z : z = \left(\mathbf{FAF}^{-1}\mathbf{p}, \mathbf{p}\right) / (\mathbf{p}, \mathbf{p})\}. \tag{3.10}$$

The numerical range is the convex hull of the spectrum for a normal operator (and is therefore always in the stable half plane $z_r < 0$ for a stable operator) , but can extend significantly to even protrude into the unstable half-plane $z_r > 0$ for stable non-normal operators. Its maximum protrusion is equal to the numerical abscissa and thus determines the maximum energy growth rate at $t = 0^+$.

4. Non-modal analysis: results

4.1. *Transient growth and numerical range*

In figure 2, we show the optimal growth of the interfacial energy $G^{\max}_{\Delta S}(T)$ for viscosity of ratios $\lambda = 0.5$ and 5, varying the capillary number Ca. The threshold value of Ca to yield transient growth is between 4 and 5, in accordance with the rightmost boundary of the numerical range (see inset) depicted in the complex plane (z_r, z_i). The boundary is almost tangent to $z_r = 0$ at Ca ≈ 4.9 for $\lambda = 0.5$ and Ca ≈ 4.53 for $\lambda = 5$ representing the critical capillary number $\mathrm{Ca_c}$ above which the maximum energy growth rate at $t = 0$, $\max_{\mathbf{f}(0)} \frac{1}{\sqrt{\Delta S}}\frac{d\sqrt{\Delta S}}{dt}|_{t=0^+}$, is positive, guaranteeing transient growth.

4.2. *Linear growth and shape evolutions*

Non-modal analysis not only predicts the maximum energy growth over a particular time interval, but also provides the optimal perturbation, i.e. the initial shape coefficients $\mathbf{f}^{\mathrm{opt}}_{[T]}(0)$ that ensure the optimal gain at horizon T. Figure 3 depicts the individual energy gains $G_{\Delta S}$ for four optimal initial conditions $\mathbf{f}^{\mathrm{opt}}_{[T]}(0)$ corresponding to $T = 0.2$, 1.05, 3.95 and 5.45, with $\lambda = 0.5$ and Ca $= 6$. Their gain profiles are tangent to $G^{\max}_{\Delta S}(T)$ at $t = T$. The optimal perturbation targeting $T = T_{\max} = 2.95$ coincides with the optimal growth $G^{\max}_{\Delta S}$ at its peak.

Assuming small deformation amplitude and integrating equ. 2.4 in time, the linear

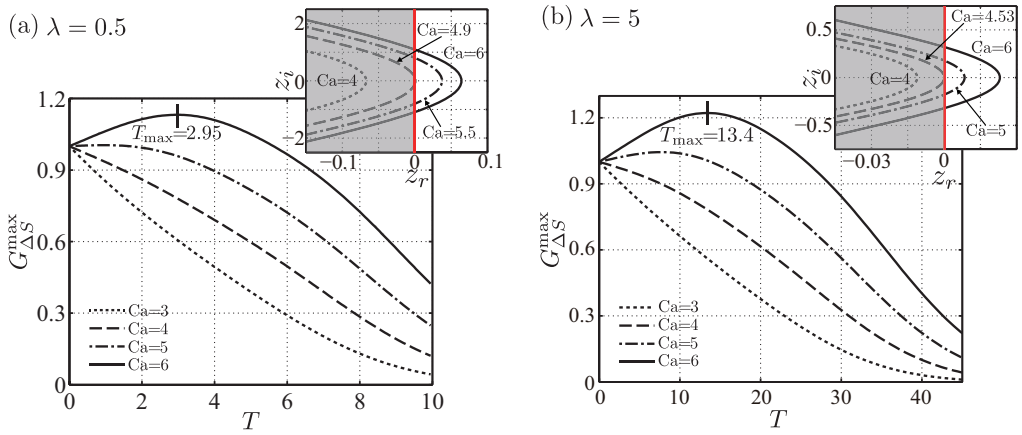

Figure 2: The optimal growth of the interfacial energy $G^{\max}_{\Delta S}(T)$ versus the nondimensional time T, for viscosity ratio $\lambda = 0.5$ (a) and $\lambda = 5$ (b); for each case, four capillary number Cas are shown and for the highest Ca, the time $T_{\max}$ corresponding to the peak energy growth is marked. The inset shows the boundary of the numerical range (z_r, z_i).

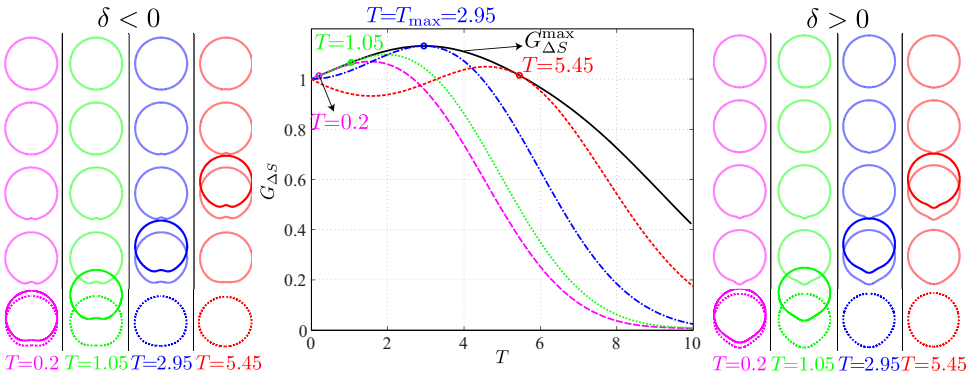

Figure 3: Linear growth $G_{\Delta S}$ of the interfacial energy of the droplets with an optimal initial perturbation $\mathbf{f}^{\text{opt}}_{[T]}(0)$ for the target times $T = 0.2$, 1.05, 2.95 and 5.45; the solid curve indicates the optimal growth $G^{\max}_{\Delta S}(T)$ and it reaches its peak at $T = T_{\max} = 2.95$. The linear shape evolution of the perturbations are shown for negative and positive δ, on the left and right panel respectively.

shape evolution is readily reconstructed for the droplets with the four optimal initial conditions, depicted in figure 3, at time $t = 0$ (dashed), $2.5, 5, 7.5, 10$ (light solid) and the target time $t = T$ (solid); the evolution is shown for negative/positive δ in (a)/(c). For both signs, the initial perturbation is mainly introduced near the tail ($\theta = 0$) of the droplet where the interface is respectively flattened for $\delta < 0$ and stretched for $\delta > 0$ while the front part of the droplet remains spherical. In accordance with the modal analysis implying a linearly stable evolution, the perturbations eventually decay and the droplets finally recover a spherical shape.

5. Nonlinear analysis

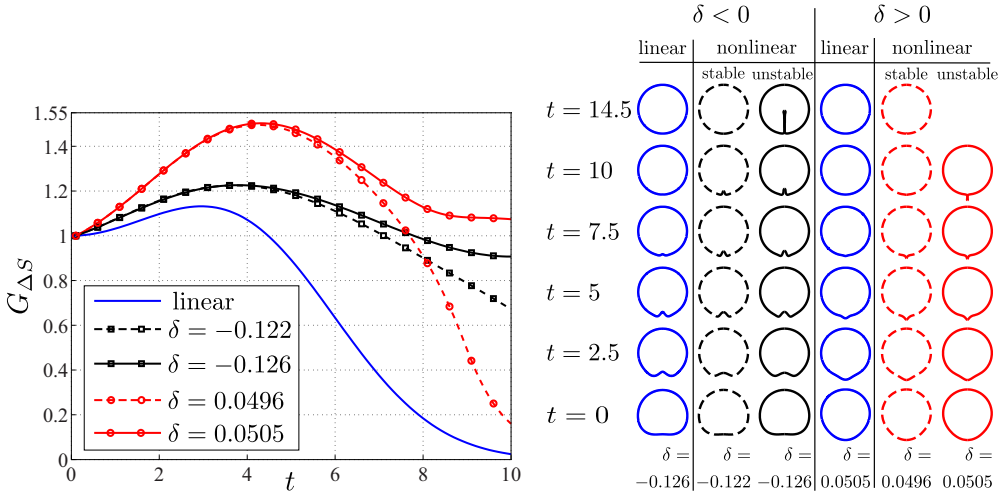

(a) Energy growth $G_{\Delta S}(t)$ (b) Shape evolution

Figure 4: (a): Nonlinear energy growth $G_{\Delta S}$ of the droplets with the optimal perturbation $\mathbf{f}^{\text{opt}}_{[T]}(0)$ for the target time $T = T_{\max} = 2.95$; the solid curve indicates the linear energy growth. For positive δ, $G_{\Delta S}$ of droplets with $\delta = 0.0496$ and 0.0505 are shown, the former/latter being stable/unstable; for negative δ, the chosen value leading to stable and unstable evolution is $\delta = -0.122$ and $\delta = -0.126$ respectively. (b): The shape evolutions of the corresponding droplets.

5.1. *Nonlinear energy growth and shape evolution using DNS*

As the droplets deform more and more on increasing the initial perturbation amplitude, nonlinearities become significant and the droplet evolution cannot be adequately described by the linearised equations. We resort to DNS to address the non-linear dynamics using a three-dimensional axisymmetric boundary integral implementation, following the standard approach of Koh & Leal (1989).

We focus on the droplets of $\lambda = 0.5$ and $\text{Ca} = 6$ with the optimal perturbation $\mathbf{f}^{\text{opt}}_{[T_{\max}]}(0)$ achieving the peak of the optimal energy growth $G^{\max}_{\Delta S}$ at $T_{\max}$. Two slightly different magnitudes of perturbation $\delta = 0.0496, 0.0505$ are chosen for the positive δ and similarly $\delta = -0.122, -0.126$ for the negative case. Their energy growth $G_{\Delta S}(t) = \sqrt{\frac{\Delta S(t)}{\Delta S(0)}}$ is plotted in figure 4(a), together with the linear counterpart $G_{\Delta S}(t)$ using equ. 3.3. The linear and non-linear energy growth share the same trend in the initial growing phase $t < 3$, but differ as the former is approximated by a truncated Taylor expansion. For the two values of δ with the same sign but slightly different magnitude, the energy growth curves almost collapse before reaching their peaks at $t \approx 4$, but diverge afterwards; $G_{\Delta S}$ decays for the smaller magnitudes $\delta = -0.122$ and $\delta = 0.0496$ indicating stable evolutions but maintains a sustained value around 1 for larger initial amplitudes $\delta = -0.126$ and $\delta = 0.0505$, implying the onset of instability.

The shape evolutions of droplets are shown in figure 4(b). For $\delta = -0.122$ and -0.126, no significant difference is observed for $0 < t < 7.5$: an inward cavity develops at the rear and sharpens; it is subsequently smoothed out and disappears for $\delta = -0.122$ while it keeps growing to form a long indentation for $\delta = -0.126$. These two values of δ bound a threshold initial amplitude required to excite nonlinear instabilities. A similar trend

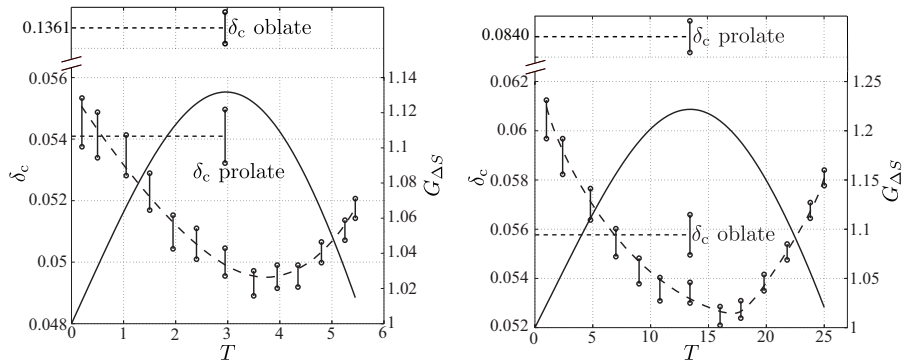

(a) $(\lambda, \mathrm{Ca}) = (0.5, 6)$ (b) $(\lambda, \mathrm{Ca}) = (5, 6)$

Figure 5: The critical perturbation magnitude δ_c for: (a): $(\lambda, \mathrm{Ca}) = (0.5, 6)$ and (b): $(\lambda, \mathrm{Ca}) = (5, 6)$. The upper and lower limits of δ_c (measured by the left scale) are plotted versus the target time T, with a curve fitted to show the trend. Accordingly, the linear energy growth $G_{\Delta S}$ (measured by the right scale) is provided. δ_c^P and δ_c^O is the critical magnitude for an initially prolate and oblate respectively.

is found for positive values of δ, while the instability arises through the formation of a dripping tail.

It becomes natural to introduce δ_c, the critical magnitude of the perturbation above/below which the evolution of the drop is unstable/stable. Parametric computations are conducted to identify $\delta_c^{\pm}$ within a confidence interval (for instance $\delta_c^+ \in [0.0496, 0.0505]$ and $\delta_c^- \in [-0.122, -0.126]$ as in figure 4(a)). Searching in both directions, the critical amplitude is then defined as $\delta_c = \min(|\delta_c^+|, |\delta_c^-|)$. When $\lambda = 0.5$ and $\mathrm{Ca} = 6$, $|\delta_c^-| > |\delta_c^+|$, implying that the instability tends to favour an initially stretched tail with respect to a flattened bottom; otherwise when $\lambda = 5$ the situation reverses ($|\delta_c^-| < |\delta_c^+|$), as discussed in next section.

5.2. *Critical amplitude of the perturbation* δ_c

Following the description of the previous paragraph, the critical deformation amplitude $\delta_c(T)$ can be determined for any targeting time T and associated optimal initial perturbation $\mathbf{f}_{[T]}^{\mathrm{opt}}(0)$. The critical deformation amplitude $\delta_c(T)$ is plotted in figure 5 for $\mathrm{Ca} = 6$ and both $\lambda = 0.5$ and $\lambda = 5$, together with the optimal growth $G_{\Delta S}^{\max}$. The critical deformation amplitude δ_c is negatively correlated with $G_{\Delta S}^{\max}$ and corresponds to a target time T slightly larger than $T_{\max}$ where the peak transient growth is reached. This shows that the transient growth reduces the threshold non-linearity needed to trigger instabilities and consequently the critical magnitude of the initial perturbation.

We also determined the critical amplitude $\delta_c^{P/O}$ for an initially prolate (P) / oblate (O) ellipsoidal droplet to be unstable, as reported in figure 5. When the fluid inside the droplet is less viscous than the one outside, i.e. $\lambda < 1$, an initially prolate droplet is more unstable, δ_c^P is less than half that of an oblate droplet δ_c^O; the trend reverses as $\lambda > 1$. Such an observation is in agreement with the results of Koh & Leal (1989) using DNS (see fig. 11 of their paper). As expected, the minimum δ_c using the optimal perturbations is smaller than $\min(\delta_c^P, \delta_c^O)$ based on the limited family of ellipsoidal shapes.

So far, we have analysed the critical amplitude δ_c of perturbations exhibiting transient energy growth. We would like to know how it varies as the transient growth decreases and even disappears as it is suppressed by high surface tension. In addition to $\mathrm{Ca} = 6$, the

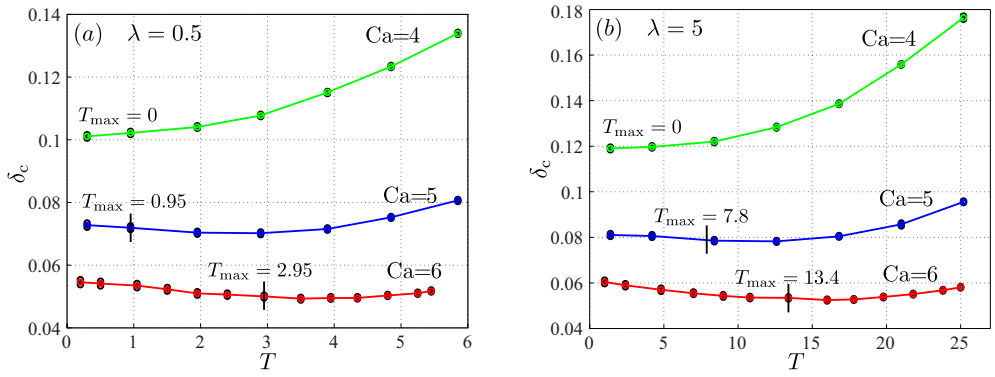

Figure 6: Akin to figure 5, adding δ_c of two smaller Cas for (a): $\lambda = 0.5$ and (b): $\lambda = 5$.

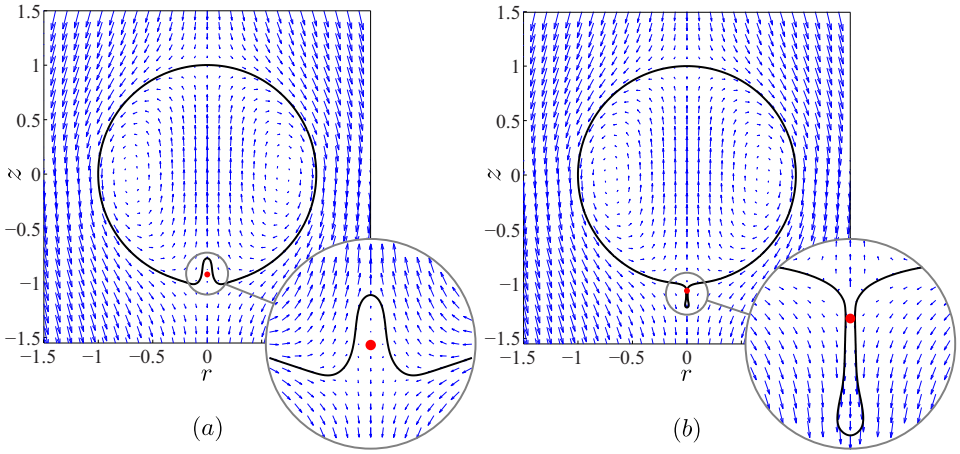

Figure 7: The flow field co-moving with the droplet, using the optimal initial coefficient $\mathbf{f}^{\mathrm{opt}}_{[T_{\max}]}(0)$, when $(\lambda, \mathrm{Ca}) = (0.5, 6)$, (a): $\delta = -0.126$ and (b): $\delta = 0.0505$. The red dot indicates the stagnation point of the flow.

time-dependence of δ_c is shown in figure 6 for $\mathrm{Ca} = 4, 5$. As expected, δ_c increases with decreasing Ca, by a factor of approximately 3, varying from the highest to the lowest Ca. With respect to T, δ_c varies non-monotonically for $\mathrm{Ca} = 5, 6$ showing transient growth. In the absence of transient growth, like for $\mathrm{Ca} = 4$, δ_c increases with T monotonically. Indeed, without transient growth, the energy decays monotonically and $T_{\max} = 0$, hence the minimum δ_c appears at $T \approx 0$.

6. Conclusion and discussions

In this paper, we have performed non-modal analysis and DNS to investigate the shape instabilities of an intertialess rising droplet which tends to recover the spherical shape, the attractor solution, due to surface tension. For sufficiently low surface tension, transient growth of the interfacial energy arises and leads to a bypass transition. This reduces the initial disturbance amplitude required to trigger instability, hence significantly decreasing the threshold magnitude of perturbation for the droplet to escape the basin of attraction. This magnitude is negatively correlated to the optimal growth of the interfacial energy.

We now compare our results with the work of Koh & Leal (1989) who employed DNS to identify the critical capillary number $\mathrm{Ca_c}$ leading to shape instabilities of an initially prolate or oblate ellipsoidal sedimenting droplet; the magnitude of perturbation is $\Delta = \frac{L-B}{L+B}$ (see figure 1). For their lowest magnitude $|\Delta| = 1/21$ considered, $\mathrm{Ca_c} \in (4, 5)$ for $\lambda = 0.1, 0.5$ and 5, indeed close to our prediction: $\mathrm{Ca_c} \approx 5.42, 4.9$ and 4.53 respectively for the same λ. Additionally, Koh & Leal (1989) observed that for a viscosity ratio $\lambda < 1/\lambda > 1$, the first unstable pattern appears as a protrusion/indentation developing near the tail of the droplet that is initially a prolate/oblate. The trend holds in our case even though we search over all possibilities for the most 'dangerous' initial perturbation instead of using an initially ellipsoidal shape. This is also reflected from the initial shapes: as $\lambda < 1/\lambda > 1$, the optimal shape shares a common feature with an oblate/prolate ellipsoid, namely its rear interface is compressed/stretched.

To explain the dependence of the instability patterns on the viscosity ratio λ, let us focus on the velocity field near the tail of the droplet (see figure 7), where the flow resembles a uniaxial extensional flow, drawing the tip into the drop on the top side and pulling it outwards on the other side. We suggest that this imbalance induces the onset of the shape instability. The internal (respectively external) viscous force on the tip is $\mu_1 \partial u_z^{\mathrm{tip}}/\partial z$ (respectively $\mu_2 \partial u_z^{\mathrm{tip}}/\partial z$). When $\mu_1 < \mu_2$, i.e. $\lambda < 1$, the external viscous effect overcomes the internal one, hence the perturbation tends to be stretched outward to form a protrusion; otherwise, when $\lambda > 1$, it is prone to be sucked inwards to form an indentation.

Developed originally for hydrodynamic stability analysis, non-modal tools have here demonstrated the predictive capacity for the inertialess shape instabilities of capillary interfaces. This work might stimulate the application of non-modal analysis for complex multiphase flow instabilities even at low Reynolds number.

Acknowledgements

L.Z. thanks Francesco Viola for the helpful discussions. We thank the anonymous referee for pointing out an incorrect coefficient in our previous derivation. Computer time from SCITAS at EPFL is acknowledged, and the European Research Council is acknowledged for funding the work through a starting grant (ERC SimCoMiCs 280117).

REFERENCES

Baggett, J. S., Driscoll, T. A. & Trefethen, L. N. 1995 A mostly linear model of transition to turbulence. *Phys. Fluids* **7** (4), 833–838.

Balasubramanian, K. & Sujith, R. I. 2008 Thermoacoustic instability in a rijke tube: Non-normality and nonlinearity. *Phys. Fluids* **20** (4), 044103.

Batchelor, George Keith 2000 *An introduction to fluid dynamics*. Cambridge university press.

Bertozzi, A. L. & Brenner, M. P. 1997 Linear stability and transient growth in driven contact lines. *Phys. Fluids* **9** (3), 530–539.

de Bruyn, J. R. 1992 Growth of fingers at a driven three-phase contact line. *Phys. Rev. A* **46** (8), R4500.

Davis, J. M. & Troian, S. M. 2003 On a generalized approach to the linear stability of spatially nonuniform thin film flows. *Phys. Fluids* **15** (5), 1344–1347.

Hadamard, J. 1911 Mouvement permanent lent d'une sphère liquide et visqueuse dans un liquide visqueux. *C. R. Acad. Sci. Paris* **152**, 1735–1738.

Huppert, H. E. 1982 Flow and instability of a viscous current down a slope. *Nature* **300** (5891), 427–429.

Johnson, Robert A & Borhan, Ali 2000 Stability of the shape of a surfactant-laden drop translating at low reynolds number. *Physics of Fluids (1994-present)* **12** (4), 773–784.

Jovanović, M. R. & Kumar, S. 2010 Transient growth without inertia. *Phys. Fluids* **22** (2), 023101.

Juniper, M. P. 2011 Triggering in the horizontal rijke tube: non-normality, transient growth and bypass transition. *J. Fluid Mech.* **667**, 272–308.

Koh, C. J. & Leal, L. G. 1989 The stability of drop shapes for translation at zero reynolds number through a quiescent fluid. *Phys. Fluids* **1** (8), 1309–1313.

Kojima, M., Hinch, E.J. & Acrivos, A. 1984 The formation and expansion of a toroidal drop moving in a viscous fluid. *Phys. Fluids* **27** (1), 19–32.

Leal, L. G. 2007 *Advanced transport phenomena: fluid mechanics and convective transport processes*. Cambridge University Press.

Reddy, S. C. & Henningson, D. S. 1993 Energy growth in viscous channel flows. *J. Fluid Mech.* **252**, 209–238.

Rybzynski, W. 1911 Über die fortschreitende Bewegung einer flüssingen Kugel in einem zähen Medium. *Bull. Int. Acad. Sci. Cracovie* **1A**, 40–46.

Schmid, P. J. 2001 Tools for nonmodal stability analysis. *Notes from a Ladhyx Tutorial* p. 24.

Schmid, P. J. 2007 Nonmodal stability theory. *Annu. Rev. Fluid Mech.* **39**, 129–162.

Schmid, P. J. & Henningson, D. S. 2001 *Stability and transition in shear flows*, *Applied Mathematical Sciences*, vol. 142. New York: Springer-Verlag.

Trefethen, L. N. & Embree, M. 2005 *Spectra and pseudospectra: the behavior of nonnormal matrices and operators*. Princeton University Press.

Trefethen, L. N., Trefethen, A. E., Reddy, S. C. & Driscoll, T. A. 1993 Hydrodynamic stability without eigenvalues. *Science* **261** (5121), 578–584.

Wu, H, Haj-Hariri, H & Borhan, A 2012 Stability of the shape of a translating viscoelastic drop at low reynolds number. *Physics of Fluids (1994-present)* **24** (11), 113101.